Research Article | Vol. 13, No. 5 / 1 May 2022 / Biomedical Optics Express 2695
Biomedical Optics EXPRESS

Photoacoustic microscopy of vascular adaptation and tissue oxygen metabolism during cutaneous wound healing

NAIDI SUN,[1,2] ANTHONY C. BRUCE,[1] BO NING,[1] RUI CAO,[1] YIMING WANG,[1] FENGHE ZHONG,[1,2] SHAYN M. PEIRCE,[1] AND SONG HU[1,2,*]

[1]Department of Biomedical Engineering, University of Virginia, Charlottesville, VA 22908, USA
[2]Department of Biomedical Engineering, Washington University in St. Louis, St. Louis, MO 63130, USA
[*]songhu@wustl.edu

Abstract: Cutaneous wounds affect millions of people every year. Vascularization and blood oxygen delivery are critical bottlenecks in wound healing, and understanding the spatiotemporal dynamics of these processes may lead to more effective therapeutic strategies to accelerate wound healing. In this work, we applied multi-parametric photoacoustic microscopy (PAM) to study vascular adaptation and the associated changes in blood oxygen delivery and tissue oxygen metabolism throughout the hemostasis, inflammatory, proliferation, and early remodeling phases of wound healing in mice with skin puncture wounds. Multifaceted changes in the vascular structure, function, and tissue oxygen metabolism were observed during the 14-day monitoring of wound healing. On the entire wound area, significant elevations of the arterial blood flow and tissue oxygen metabolism were observed right after wounding and remained well above the baseline over the 14-day period. On the healing front, biphasic changes in the vascular density and blood flow were observed, both of which peaked on day 1, remained elevated in the first week, and returned to the baselines by day 14. Along with the wound closure and thickening, tissue oxygen metabolism in the healing front remained elevated even after structural and functional changes in the vasculature were stabilized. On the newly formed tissue, significantly higher blood oxygenation, flow, and tissue metabolism were observed compared to those before wounding. Blood oxygenation and flow in the new tissue appeared to be independent of when it was formed, but instead showed noticeable dependence on the phase of wound healing. This PAM study provides new insights into the structural, functional, and metabolic changes associated with vascular adaptation during wound healing and suggests that the timing and target of vascular treatments for wound healing may affect the outcomes.

1. Introduction

Every demographic of the population is at the risk of suffering cutaneous wounds, which include puncture wounds, ulcers, and contusions caused by burn, prolonged pressure, vascular pathologies, or accidents. In 2014, 8.2 million people in the United States experienced episodes of care for one or more of these outcomes [1], especially for the patients with pressure, venous stasis, or diabetes mellitus [2].

Because of the strong clinical relevance and associated economic burden, mechanisms of wound healing have been widely studied for decades [3–6], from which revascularization of the wound bed has been found to be tightly linked to the clinical outcomes of wound healing [3,7–10]. Moreover, recent studies have shown that angiogenesis in the wound healing front is important to the healing process [11–13]. To understand vascular adaptation during wound repair and tissue regeneration [14–16], a variety of imaging technologies have been developed or adopted, including dermoscopy [17,18], confocal microscopy [19,20], laser speckle contrast imaging

#456198 https://doi.org/10.1364/BOE.456198
Journal © 2022 Received 14 Feb 2022; revised 30 Mar 2022; accepted 31 Mar 2022; published 8 Apr 2022

Biomedical Optics EXPRESS

[21,22], two-photon microscopy [23–25], ultrasound imaging [26,27], and optical coherence tomography [28–30]. However, it remains incompletely understood how vascular adaptation changes blood oxygen delivery and tissue metabolism during wound healing, mainly due to technical limitations.

Exploiting the optical absorption of blood hemoglobin, photoacoustic microscopy (PAM) has demonstrated great promise for label-free and noninvasive imaging of the microvasculature [31–34]. Using conventional PAM, previous studies have reported changes in vascular structure and oxygen saturation of hemoglobin (sO_2) during wound healing [35–37]. In this work, we extended the study to vascular hemodynamics and tissue oxygen metabolism by integrating the multi-parametric PAM and quantitative analysis. Specifically, we longitudinally monitored the healing process of a cutaneous puncture wound in the mouse ear over a 14-day time period, which spanned the hemostasis phase (i.e., shortly after wounding), inflammatory phase (i.e., one day after wounding), proliferation phase (i.e., the first 7 days after wounding), and early remodeling phase (i.e., 7 to 14 days after wounding) [4]. Combining the time-lapse microscopic imaging and quantitative analysis, we characterized the spatiotemporal profiles of vascular adaptation (i.e., vessel diameter and perfused vascular area) to wound healing (i.e., wound area and healing front thickness) and the attendant changes in vascular hemodynamics (hemoglobin concentration (C_{Hb}), sO_2, and blood flow) and tissue oxygen metabolism (i.e., oxygen extraction fraction (OEF) and metabolic rate of oxygen (MRO_2)).

2. Methods

2.1. PAM imaging of the mouse ear

As shown in Fig. 1, two nanosecond-pulsed lasers (wavelength: 532 nm and 558 nm; repetition rate: 8.5 kHz; pulse energy: 80 nJ on the tissue surface) were used for optical excitation. After two neutral-density filters (NDF; Thorlabs, NDC-50C-2M), the two beams were combined via a dichroic beam splitter (DBS; Semrock, FF552-Di02-25 × 36), and coupled into a single-mode optical fiber (SMF; Thorlabs, P1-460B-FC-1) through an objective lens (Newport, M-10X). To compensate for the intensity fluctuation of the laser, ~5% of the light was picked off by a beam sampler (BSA; Thorlabs, BSF10-A) and monitored by a highspeed photodiode (PD; Thorlabs, FDS100). In the scanning head, the output of the SMF was collimated by an achromatic doublet (DL; Thorlabs, AC127-025-A), and then focused by another identical doublet and a correction lens (CL; Thorlabs, LA1207-A) onto the imaging object. A customized ring-shaped ultrasonic transducer (inner diameter: 2.2 mm; outer diameter: 4.0 mm; focal length: 6.0 mm; center frequency: 35 MHz; 6-dB intensity bandwidth: 70%) was used for ultrasonic detection. Details of the multi-parametric PAM system utilized in this study has been previously reported [38].

Four hairless SKH1-Hrhr mice (Charles River, 6-week-old male) were maintained under anesthesia using 1.0–1.5% inhaled isoflurane, and the body temperature was kept at 37 °C using a temperature-controlled (Cole-Parmer, EW-89802-52) heating pad (Omega, SRFG-303/10) on an animal holder. A layer of ultrasound gel (~1 mm) was applied on the surface of the mouse ear for acoustic coupling. The gel was in gentle contact with the bottom of a water tank, which contained temperature-maintained (37 °C) deionized water. After the baseline PAM images were acquired (i.e., prior to wounding), a 0.8-mm biopsy punch (Miltex, Integra LifeSciences) was used to create an excisional punch wound at the center of the right ear. To serially monitor the wound-induced structural and functional changes in the vasculature, a 3.5×2.5 mm^2 region of interest enclosing the wounded area was repeatedly imaged before, after, and up to 14 days following wounding. Each image was acquired with step sizes of 0.1 μm and 10 μm along the x- and y-direction, respectively. The acquisition time was ~20 minutes. All animal procedures were performed in accordance with the protocols approved by the University of Virginia Animal Care and Use Committee.

Biomedical Optics EXPRESS

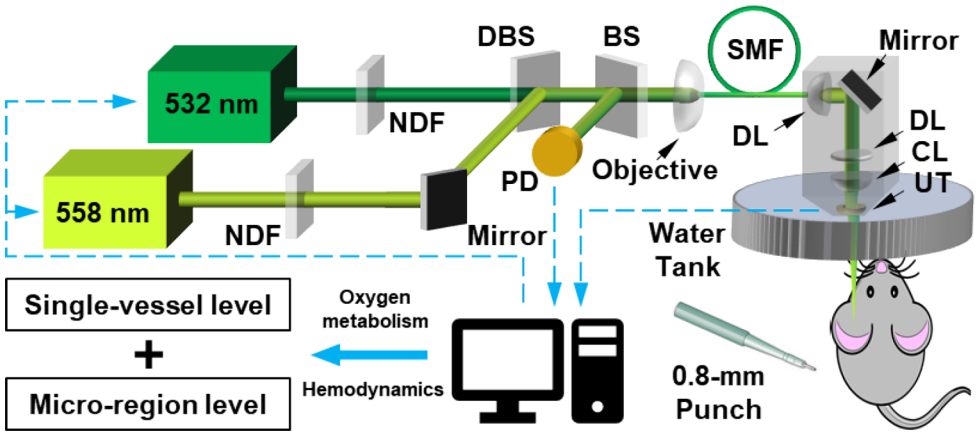

Fig. 1. Schematic of the multi-parametric PAM. NDF, neutral-density filter; DBS, dichroic beamsplitter; PD, photodiode; BS, beam sampler; SMF, regular single-mode fiber; DL, doublet; CL, correction lens; UT, ring-shaped ultrasonic transducer.

2.2. Quantification of wound, vascular, and oxygen-metabolic parameters

Two wound parameters, including the wound area and the healing front thickness, were quantified based on the three-dimensionally resolved PAM images. First, the puncture wound was identified by manually segmenting out the region with no vascular/tissue coverage in the projection images (e.g., the 'dark holes' in Fig. 2(a)-(d)), based on which the area was quantified. Then, the healing front thickness could be obtained from the B-scans (e.g., Fig. 2(e)), based on the depth-resolved ultrasonic detection.

In the multi-parametric PAM, simultaneous quantification of C_{Hb}, sO_2, and blood flow is achieved by analyzing the amplitude fluctuation due to the Brownian motion of erythrocytes, the differential absorption of oxy- and deoxy-hemoglobin at the two different wavelengths, and the decorrelation of successively acquired A-lines due to blood flow, respectively. With the aid of our previously reported semi-automatic segmentation approach [38–41], the structural and functional parameters of the microvasculature can be extracted at the single-vessel level.

The following formulas were used for the derivation of volumetric flow ($Flow_v$), OEF, and MRO_2:

$$Flow_v = \pi v d^2/8,$$

$$OEF = (s_aO_2 - s_vO_2)/s_aO_2\,, \text{ and}$$

$$MRO_2 = \xi \times C_{Hb} \times s_aO_2 \times OEF \times Flow_v,$$

where d is the vascular diameter, and v is the peak flow speed along the vascular axis; s_aO_2 and s_vO_2 are the sO_2 values of the feeding arteries and draining veins, respectively [42]; ξ is the oxygen binding capacity of hemoglobin (0.014 L O_2 per gram hemoglobin).

For the wound boundary detection, we first generated a microvessel density map. Briefly, the microvasculature was isolated by removing the non-vessel background as well as trunk arteries and veins. Then, the number of pixels occupied by the microvasculature was obtained, based on which the microvessel density was computed by taking the ratio of the microvascular pixel number to the total pixel number. Since the microvessel density of the wound site is close to zero, the wound boundary could be finally identified by applying an appropriate threshold of the microvessel density.

Biomedical Optics EXPRESS

2.3. Statistical analysis

Two-way repeated measures ANOVA was used to compare the vascular and oxygen-metabolic responses throughout the hemostasis, inflammatory, proliferation, and early remodeling phases (Fig. 3). The parameters within the healing front (Fig. 4) and newly formed tissue (Fig. 5) were compared using Two-way ANOVA. Note that a parametric or non-parametric test was selected based on a Kolmogorov–Smirnov test for normality to assess if the data followed a normal distribution. In all analyses, $p < 0.05$ was considered significant. All data were presented as mean ± standard deviation.

3. Results

3.1. Longitudinal multi-parametric PAM imaging of cutaneous wound healing

Multi-parametric images of the C_{Hb}, sO_2, and blood flow speed were acquired before (i.e., baseline) and up to 14 days following the induction of wound in the mouse ear (Fig. 2(a)–(c)). As shown in the C_{Hb} images (Fig. 2(a)), which delineated the blood-perfused vasculature, bleeding at the edge of the wound was observed right after (i.e., 5–10 mins) the induction of the puncture injury (dashed white circle in Fig. 2(a)). One day later, a clear boundary between the wound area and the healing front was observed, due to the formation of blood clot at the injury site and the clearance of debris from the damaged tissue. Additionally, capillary angiogenesis and vascular dilation within the healing front were observed on day 1 and day 7, but returned to the baseline levels on day 14. As shown in the sO_2 images (Fig. 2(b)), both the draining veins (blue arrows) and capillaries surrounding the wound showed immediate increases in blood oxygenation right after wounding, which continued to day 1 but gradually recovered to the baseline levels from days 7 to 14. In contrast, there was no significant sO_2 change in the feeding arteries (red arrows) in response to wounding. Changes in blood flow speed accompanied that in sO_2 (Fig. 2(c)). Both arterial and venous blood flow speed showed significant increases up to day 7, but returned to the baseline levels by day 14. Based on the time-of-flight acoustic detection of PAM, the tissue height maps (Fig. 2(d)), as well as the representative cross-sectional images (i.e., B-scan, Fig. 2(e)) over the white dashed line in Fig. 2(d), were obtained—revealing a sustained increase in the thickness of the healing front up to 14 days after wounding. Some collateral vessels that were poorly perfused and barely visible before wounding (white arrows in Fig. 2(a)) were recruited for hemodynamic redistribution afterward, providing additional blood supply to support the wound healing process. Interestingly, most of the collateral vessel recruitments were transient and disappeared during the early remodeling phase, but some collaterals remained recruited on day 14, highlighting the heterogeneity of vascular adaptation for hemodynamic redistribution during wound healing. Such heterogeneity was also observed in the tissue-level maps of OEF, $Flow_v$, and MRO_2 (Fig. 2(f) to (h)).

3.2. Structural and functional adaptation of feeding and draining vessels during wound healing

For quantitative analysis, the feeding arteries and draining veins of the ear vasculature (red and blue arrows in Fig. 2(b), respectively) were segmented, based on which multiple functional and metabolic parameters were quantified, including the vessel diameter, C_{Hb}, sO_2, blood flow speed, OEF, $Flow_v$, and MRO_2. To accommodate the dependence of the parameters on the vessel type, some analyses were performed separately on arteries and veins.

As shown in Fig. 3(a), the wound area changed significantly across the four stages of wound healing (showing a dramatic decrease from 0.50 mm^2 right after wounding to 0.07 mm^2 on day 14), which affirmed previous observations [28]. The largest wound area (0.67 mm^2) appeared on day 1 mainly due to clearance of debris from the punched hole. Defined as the thickest part of the wound site, the healing front thickness increased on day 1 and remained elevated on day 7

Biomedical Optics EXPRESS

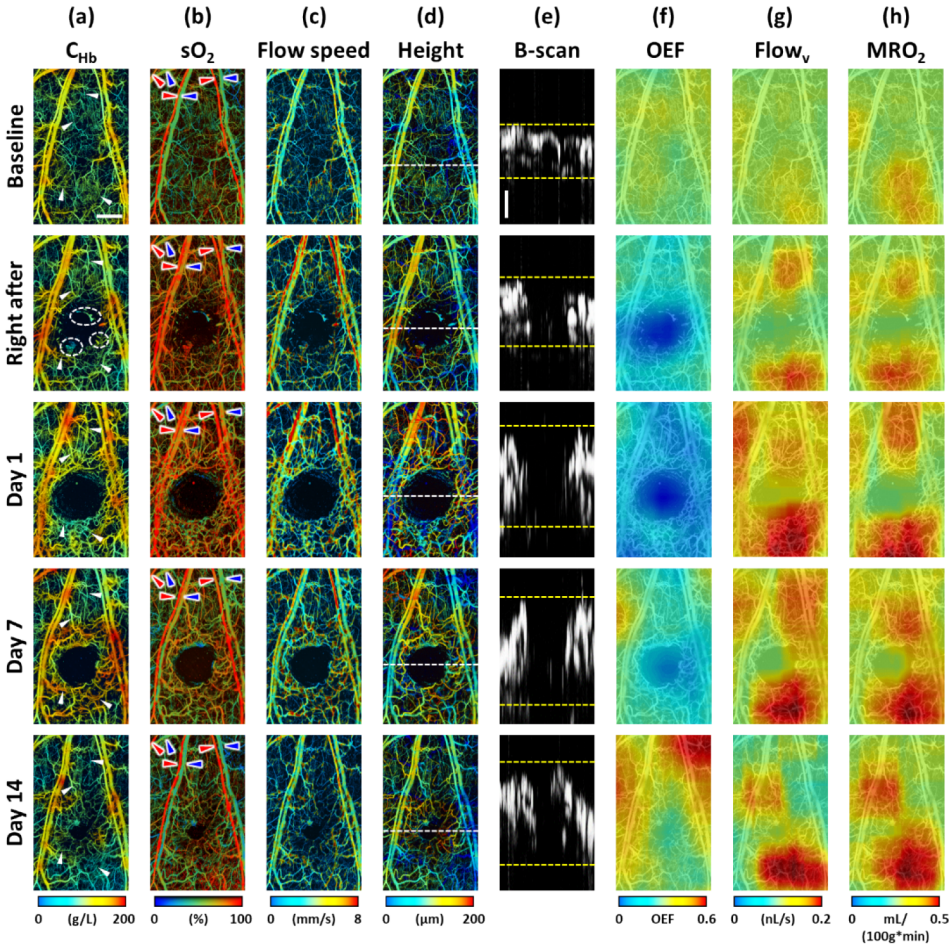

Fig. 2. Longitudinal comprehensive PAM assessments of structural, functional, and oxygen-metabolic changes in the vascular tissue during wound healing, including (a) the hemoglobin concentration (C_{Hb}), (b) the oxygen saturation of hemoglobin (sO_2), (c) blood flow speed, (d–e) tissue height and thickness, (f) oxygen extraction fraction (OEF), (g) volumetric blood flow ($Flow_v$), and (h) the metabolic rate of oxygen (MRO_2). White arrows in (a): vessels remodeled after inducing the puncture wound in the mouse ear. Dashed white circles in (a): hemorrhage. Red and blue arrows in (b): feeding arteries and draining veins analyzed in Fig. 3, respectively. The "0" position in (d) denotes the bottom of the ear vasculature. The locations of the B-scans in (e) are indicated by the white dashed lines in (d). Horizontal scale bar in (a): 500 μm. Vertical scale bar in (e): 50 μm.

Biomedical Optics EXPRESS

(199.3 μm and 199.6 μm, respectively), but decreased to 160.8 μm on day 14 (Fig. 3(b)). No changes were observed in the diameters of draining veins throughout the 14-day monitoring; but significant changes were observed in the feeding arteries (Fig. 3(c)). Specifically, the arteries showed significant dilation in the first 7 days after wounding, with a maximum change on day 1 (139.0%, $p < 0.0001$), and then returned to its baseline value on day 14 (105.9%, $p = 0.577$).

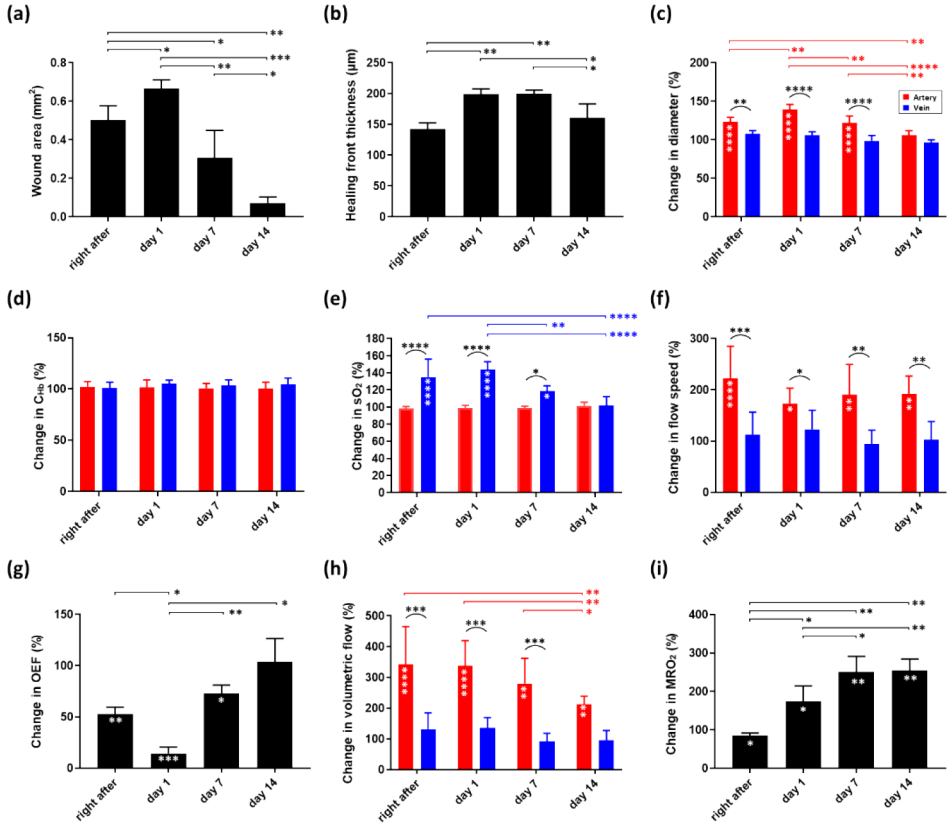

Fig. 3. (a–b) Healing of the wound tissue and associated changes in (c–f) the structure and function of the feeding arteries and draining veins of the wound area and (g–i) tissue oxygen metabolism over the 14-day monitoring. White asterisks within the bars indicate the p values between the baseline (data not shown) and the specific time point. Paired t-test was used in (a), (b), (g) and (i), while two-way ANOVA test was used in (c-f) and (h). *, **, ***, and **** represent $p < 0.05$, $p < 0.01$, $p < 0.001$, and $p < 0.0001$, respectively. Data are presented as mean ± SD. $n = 4$.

The C_{Hb} values in both arteries and veins remained unchanged throughout the monitoring period (Fig. 3(d)). While no statistically appreciable change was observed in the arterial sO_2, the venous sO_2 showed significant increases right after wounding (135.2%, $p < 0.0001$), on day 1 (144.0%, $p < 0.0001$), and on day 7 (118.6%, $p < 0.05$), and then returned to the baseline level on day 14 (102.0%, $p = 0.703$), as shown in Fig. 3(e). In contrast to the insignificant changes in the venous blood flow speed (Fig. 3(f)), the arterial blood flow speed increased immediately after wounding (223.0%, $p < 0.0001$) and remained above the baseline across the 14-day monitoring (173.2% on day 1, $p < 0.05$; 190.8% on day 7, $p < 0.01$; 191.5% on day 14, $p < 0.01$).

Because of the lack of changes in the arterial sO_2, the OEF showed an opposite trend to that of the venous sO_2 (Fig. 3(g)). Specifically, the OEF decreased immediately after wounding (52.6%, $p < 0.01$), continued to drop on day 1 (14.4%, $p < 0.001$), but then gradually recovered to the

Biomedical Optics EXPRESS

baseline level as the wound healed (72.9% on day 7, $p < 0.05$; 103.7% on day 14, $p = 0.533$). The volumetric blood flow, a parameter co-determined by the vessel diameter and blood flow speed, showed a large increase in the feeding arteries right after wounding (343.1%, $p < 0.0001$) and remained well above the baseline over time (337.8% on day 1, $p < 0.0001$; 280.4% on day 7, $p < 0.01$; 212.9% on day 14, $p < 0.01$), which was in contrast to the insignificant change in the draining veins (Fig. 3(h)). As shown in Fig. 3(i), the MRO_2 decreased immediately after wounding (85.4%, $p < 0.05$), mainly because the biopsy punch removed the tissue at the wound site, but the MRO_2 exhibited sustained increases through day 14 (174.3% on day 1, $p < 0.05$; 250.5% on day 7, $p < 0.01$; 254.9% on day 14, $p < 0.01$).

3.3. Vascular function and oxygen metabolism in the wound healing front

The high resolution of multi-parametric PAM allowed pinpointing functional and oxygen-metabolic changes that were specific to the newly regenerated tissue within the wound healing front (the red annular regions in Fig. 4(a)), which was defined as the region that was immediately proximal to the open wound with an area that was 10% of the wound area (the translucent gray circles in Fig. 4(a)) at a given time point.

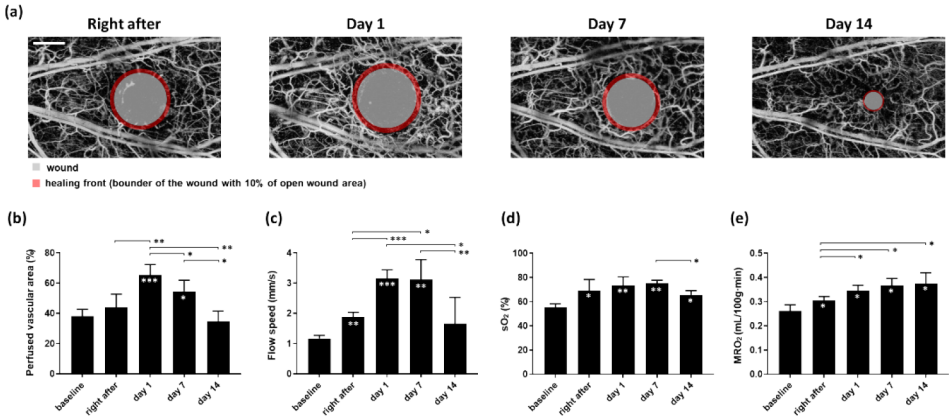

Fig. 4. (a) Illustration of wound healing process and the definition of the healing front. (b-e) Changes in perfused vascular area, flow speed, sO_2, and MRO_2 in the wound healing front. White asterisks within the bars indicate the p values between the baseline and the specific time point. Paired t-test was used for all comparisons. *, **, ***, and **** represent $p < 0.05$, $p < 0.01$, $p < 0.001$, and $p < 0.0001$, respectively. Data are presented as mean ± SD. Scale bar: 500 μm. $n = 4$.

The perfused vascular area (defined as the percentage of the healing front area covered by blood-perfused 'functional' vessels), the average sO_2 and blood flow speed of the vasculature within the healing front, and the MRO_2 of the tissue within the healing front were measured or derived. The corresponding baseline values within the wound area before the puncture injury were also quantified to provide intra-animal controls. As shown in Fig. 4(b), immediately after wounding, the perfused vascular area remained unchanged compared to the baseline level (44.1% *vs.* 38.2%, $p = 0.670$). Then, it increased abruptly on day 1 (65.3%, $p < 0.001$) and remained well above the baseline on day 7 (54.7%, $p < 0.05$), likely due to the formation of neovessels and the increase in perfusion, followed by a regression back to the baseline by day 14 (35.0%, $p = 0.403$). Similarly, the time course of blood flow speed in the healing front followed a biphasic pattern, as shown in Fig. 4(c). Specifically, the blood flow speed increased immediately after wounding (1.89 mm/s, $p < 0.01$), continued to increase on day 1 (3.16 mm/s, $p < 0.001$), remained elevated on day 7, (3.11 mm/s, $p < 0.01$), and regressed to the baseline by day 14 (1.66 mm/s, $p = 0.318$). As

Biomedical Optics EXPRESS

shown in Fig. 4(d), in contrast, the vascular sO_2 in the healing front increased immediately after wounding (69.0% *vs.* 55.7%, $p < 0.05$) and remained above the baseline throughout the 14-day monitoring (73.5% on day 1, $p < 0.01$; 75.2% on day 7, $p < 0.01$; 65.7% on day 14, $p < 0.05$), although it dropped from day 7 to day 14 ($p < 0.05$). The MRO_2 of the regenerated tissues within the wound healing front exhibited a gradual and continued increase throughout the 14 days of wound healing (0.37 mL/100g·min on day 14 *vs.* 0.26 mL/100g·min at the baseline, $p < 0.05$), as shown in Fig. 4(e).

3.4. Vascular function and oxygen metabolism in the newly formed tissue

Moreover, we quantified functional and metabolic changes of the newly formed tissue (i.e., granulation tissue) that gradually filled the open wound during the healing process. As shown in Fig. 5(a), the newly formed tissue was identified by comparing the circumferences of the open wound boundaries between two adjacent time point (i.e., the annular area bounded on the inside by the smaller circumference of the open wound at the later time point and on the outside by the larger circumference of the open wound at the earlier time point.

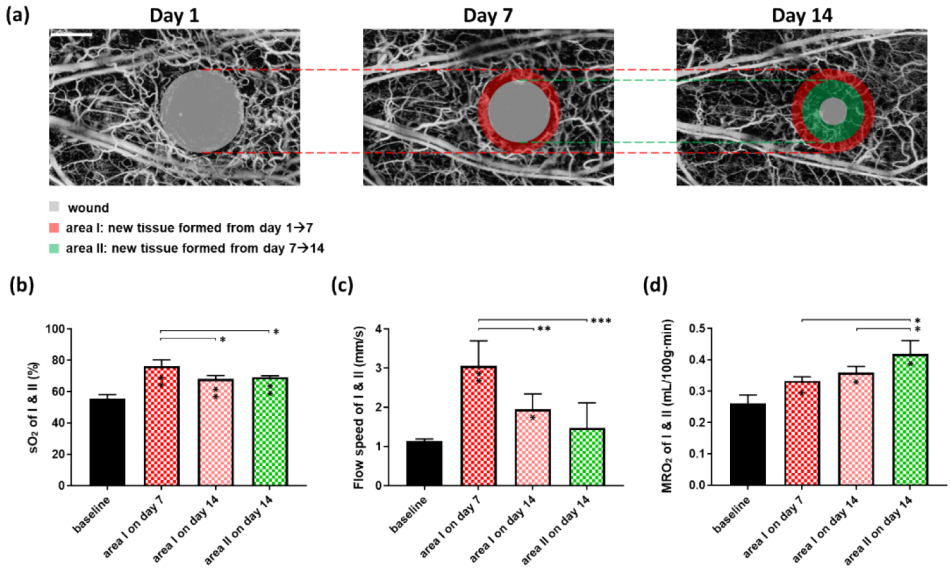

Fig. 5. (a) Illustration of the newly formed tissues. (b-d) Changes in sO_2, flow speed, and MRO_2 of the newly formed tissues during the wound healing process. Paired t-test was used for all comparisons. *, **, ***, and **** represent $p < 0.05$, $p < 0.01$, $p < 0.001$, and $p < 0.0001$, respectively. Data are presented as mean ± SD. Scale bar: 500 μm. $n = 4$.

The functional and metabolic analysis of newly formed tissue was performed at the wound site in the two pieces of new tissues formed in the first and second week after wounding, which were indicated by the translucent red and green circles, respectively (Area I and II in Fig. 5(a)). As shown in Fig. 5(b), the new tissue formed in the first week (i.e., Area I) showed a significantly higher vascular sO_2 on day 7 than the baseline value before wounding (red bar, 76.4% *vs.* 55.7%, $p < 0.01$); although slightly decreased on day 14 ($p < 0.05$), it remained above the baseline (pink bar, 68.2%, $p < 0.01$). Interestingly, the new tissue formed in the second week (i.e., Area II) did not start with a vascular sO_2 as high as that of Area I on day 7 (green bar, 69.3% *vs.* 76.4%, $p < 0.05$). Rather, it was comparable to the sO_2 of Area I on day 14 ($p = 0.863$). Compared to the sO_2, the blood flow speed in newly formed tissues were more significantly elevated over the baseline (Fig. 5(c)). In Area I, which was formed in the first week after wounding, the blood flow

Biomedical Optics EXPRESS

speed on day 7 was approximately three-fold of the baseline value (red bar, 3.06 mm/s *vs.* 1.14 mm/s, $p < 0.01$). It was followed by a significant decrease on day 14 ($p < 0.01$), but the blood flow speed in this area was still higher than the baseline value (red bar, 1.95 mm/s, $p < 0.05$). In contrast, the blood flow speed in Area II (i.e., the new tissue formed in the second week) did not show a significant difference from the baseline value on day 14 (blue bar, 1.48 mm/s, $p = 0.492$). As shown in Fig. 5(d), the MRO_2 values in the two areas of newly formed tissue were significantly higher than the baseline. Moreover, the MRO_2 of Area II measured on day 14 was even higher than those of Area I measured on both day 7 and day 14 (0.42 mL/100g·min *vs.* 0.33 and 0.36 mL/100g·min, $p < 0.05$).

4. Discussion

The state of wound oxygenation is a key determinant of wound healing outcomes [43]. The measurements of $Flow_v$ and OEF offer new insights into the oxygen supply and utilization in the wound tissue, respectively. Further, MRO_2, co-determined by the blood flow and OEF, reflects the oxygen metabolism of the wounded/regenerative tissue at the micro-regional level. All these hemodynamic and metabolic parameters are essential to understand the biology of wound healing [43–45]. Although vascular adaptation has been widely has been widely studied over decades, the underlying changes in vascular function and tissue oxygen metabolism remain incompletely understood. To fill this knowledge gap, we applied multi-parametric PAM and analytical tools to quantitatively understand the healing process of a cutaneous puncture wound in the mouse ear. We comprehensively studied the structural, functional, and oxygen-metabolic evolution of the feeding and draining vessels of the wounded area, the healing front, and the newly formed tissue over the first 14 days of wound healing, which spanned the hemostasis, inflammatory, proliferation, and early remodeling phases.

Our observations not only agree with previous reports, but also provide new insights into the evolutions of blood oxygen supply and tissue oxygen metabolism during the wound healing process. Hypoxia in the wound tissue has been previously reported, which suggests that tissue regeneration requires more oxygen than homeostasis [38,46]. The increased oxygen demand is essential for angiogenesis, tissue survival, and regrowth [44]. During the inflammatory phase, tissue hypoxia helps to activate the initial steps of wound healing by promoting reactive oxygen species activity [47] and releasing growth factors from platelets, monocytes, and endothelium [48]. During the proliferative phase, tissue hypoxia helps to increase keratinocyte motility [49] and promote angiogenesis [50]. In contrast to well-studied tissue hypoxia during wound healing, the associated changes in blood oxygen supply and tissue oxygen metabolism require a better understanding. Our study helps to bridge the knowledge gap. First, over the entire wound area, significant increases in the arterial diameter and blood flow were observed right after wounding and remained well above the baseline levels in the first 7–14 days, which suggests an increased blood oxygen supply. In addition, the PAM-based MRO_2 measurement revealed a continuous elevation of tissue oxygen metabolism throughout the 14-day time period. Second, specifically on the healing front, significant increases in the vascular density and blood flow were observed one day after wounding and remained elevated in the first 7 days of healing, before returning to the baseline levels by day 14. These structural and functional changes in the vasculature was accompanied with the significantly increased tissue MRO_2 at the healing front on day 1, which remained above the baseline throughout the monitoring. Collectively, these results suggest that vascular adaptation and associated changes in blood oxygen supply kicks in since the beginning of wound healing and remains active throughout the proliferation and early remodeling phases. Third, specifically on the newly formed tissue, significantly higher vascular sO_2, blood flow, and tissue MRO_2 were observed in comparison to the baseline levels acquired before wounding. Interestingly, the sO_2 and blood flow in the newly formed tissue appeared to be independent of when the tissue was formed; instead, they showed noticeable dependence on the healing phase.

Biomedical Optics EXPRESS

It is worth noting that the technique used in this study is optical-resolution PAM, which can resolve individual capillaries in the mouse ear. However, the microscopic resolution comes at the expense of penetration depth, which is limited to ~500 μm with visible light excitation at 532 nm. As a result, this technique may not be sufficient for studying wound healing in patients. Future developments of acoustic-resolution PAM, which penetrates multiple millimeters [51], to enable multi-parametric measurements beyond the optical diffusion limit [31] will facilitate the clinical translation of this technique.

Given that both the upstream arterial blood supply and local microcirculation are potential therapeutic targets for wound healing [50,52], the spatiotemporal changes in the blood oxygen supply to the wound area, vascular adaptations at the healing front, and oxygen metabolism of the newly formed tissue during wound healing revealed by this study suggest that the timing and target of the treatment may have important effects on the therapeutic outcomes.

5. Conclusion

In summary, we applied the multi-parametric PAM to study vascular adaptation and associated changes in blood oxygen delivery and tissue metabolism throughout the hemostasis, inflammatory, proliferation, and early remodeling phases of wound healing in mice with skin puncture wounds. Based on the serial, high-resolution, and multi-parametric measurements, we were able to quantify the changes in the vascular structure, function, and tissue oxygen metabolism throughout the multi-phase healing process and respectively on the entire wound area, wound healing front, and newly formed tissue. Our study suggests that the timing and target of vascular therapy for wound healing may affect the outcomes.

Funding. National Institutes of Health (NS099261); National Science Foundation (2023988).

Disclosures. The authors declare no conflicts of interest.

Data availability. Data underlying the results presented in this paper are not publicly available at this time but may be obtained from the authors upon reasonable request.

References

1. S. R. Nussbaum, M. J. Carter, C. E. Fife, J. DaVanzo, R. Haught, M. Nusgart, and D. Cartwright, "An economic evaluation of the impact, cost, and medicare policy implications of chronic nonhealing wounds," Value in Health **21**(1), 27–32 (2018).
2. D. Baltzis, I. Eleftheriadou, and A. Veves, "Pathogenesis and treatment of impaired wound healing in diabetes mellitus: new insights," Adv. Ther. **31**(8), 817–836 (2014).
3. A. J. Singer and R. A. F. Clark, "Cutaneous wound healing," N. Engl. J. Med. **341**(10), 738–746 (1999).
4. S. Guo and L. A. DiPietro, "Factors affecting wound healing," J. Dent. Res. **89**(3), 219–229 (2010).
5. G. Broughton, J. E. Janis, and C. E. Attinger, "The basic science of wound healing," Plastic and Reconstructive Surgery **117**(SUPPLEMENT), 12S–34S (2006).
6. A. C. de O. Gonzalez, T. F. Costa, Z. de A. Andrade, and A. R. A. P. Medrado, "Wound healing - a literature review," An. Bras. Dermatol. **91**(5), 614–620 (2016).
7. L. K. Branski, G. G. Gauglitz, D. N. Herndon, and M. G. Jeschke, "A review of gene and stem cell therapy in cutaneous wound healing," Burns **35**(2), 171–180 (2009).
8. A. Shai and H. I. Maibach, eds., *Wound Healing and Ulcers of the Skin Diagnosis and Therapy–The Practical Approach* (Springer, 2005).
9. Z. Jia, J. Gong, Y. Zeng, J. Ran, J. Liu, K. Wang, C. Xie, X. Lu, and J. Wang, "Bioinspired conductive silk microfiber integrated bioelectronic for diagnosis and wound healing in diabetes," Adv. Funct. Mater. **31**(19), 2010461 (2021).
10. L. M. Morton and T. J. Phillips, "Wound healing and treating wounds: differential diagnosis and evaluation of chronic wounds," J. Am. Acad. Dermatol. **74**(4), 589–605 (2016).
11. N. Sun, B. Ning, K. M. Hansson, A. C. Bruce, S. A. Seaman, C. Zhang, M. Rikard, C. A. DeRosa, C. L. Fraser, M. Wågberg, R. Fritsche-Danielson, J. Wikström, K. R. Chien, A. Lundahl, M. Hölttä, L. G. Carlsson, S. M. Peirce, and S. Hu, "Modified VEGF-A mRNA induces sustained multifaceted microvascular response and accelerates diabetic wound healing," Sci. Rep. **8**(1), 17509 (2018).
12. S. M. Rikard, P. J. Myers, J. Almquist, P. Gennemark, A. C. Bruce, M. Wågberg, R. Fritsche-Danielson, K. M. Hansson, M. J. Lazzara, and S. M. Peirce, "Mathematical model predicts that acceleration of diabetic wound healing is dependent on spatial distribution of VEGF-A mRNA (AZD8601)," Cell. Mol. Bioeng. **14**(4), 321–338 (2021).
13. T. N. Demidova-Rice, J. T. Durham, and I. M. Herman, "Wound Healing angiogenesis: innovations and challenges in acute and chronic wound healing," Advances in Wound Care **1**(1), 17–22 (2012).

Biomedical Optics EXPRESS

14. T. S. Stappenbeck and H. Miyoshi, "The role of stromal stem cells in tissue regeneration and wound repair," Science **324**(5935), 1666–1669 (2009).
15. G. C. Gurtner, S. Werner, Y. Barrandon, and M. T. Longaker, "Wound repair and regeneration," Nature **453**(7193), 314–321 (2008).
16. T. J. Koob, J. J. Lim, M. Massee, N. Zabek, and G. Denozière, "Properties of dehydrated human amnion/chorion composite grafts: Implications for wound repair and soft tissue regeneration," J. Biomed. Mater. Res., Part B **102**(6), 1353–1362 (2014).
17. H. Kittler, H. Pehamberger, K. Wolff, and M. Binder, "Diagnostic accuracy of dermoscopy," Lancet Oncol. **3**(3), 159–165 (2002).
18. H. Deng, C. W. P. Li-Tsang, and J. Li, "Measuring vascularity of hypertrophic scars by dermoscopy: construct validity and predictive ability of scar thickness change," Skin Res Technol **26**(3), 369–375 (2020).
19. S. González, K. Swindells, M. Rajadhyaksha, and A. Torres, "Changing paradigms in dermatology: confocal microscopy in clinical and surgical dermatology," Clin. Dermatol. **21**(5), 359–369 (2003).
20. J. O. Croxatto, A. E. Tytiun, and C. J. Argento, "Sequential in vivo confocal microscopy study of corneal wound healing after cross-linking in patients with keratoconus," J Refract Surg **26**(9), 638–645 (2010).
21. R. Mirdell, F. Iredahl, F. Sjöberg, S. Farnebo, and E. Tesselaar, "Microvascular blood flow in scalds in children and its relation to duration of wound healing: A study using laser speckle contrast imaging," Burns **42**(3), 648–654 (2016).
22. W. Heeman, W. Steenbergen, G. M. van Dam, and E. C. Boerma, "Clinical applications of laser speckle contrast imaging: a review," J. Biomed. Opt. **24**(08), 1 (2019).
23. F. A. Navarro, P. T. C. So, R. Nirmalan, N. Kropf, F. Sakaguchi, C. S. Park, H. B. Lee, and D. P. Orgill, "Two-photon confocal microscopy: a nondestructive method for studying wound healing," Plastic and Reconstructive Surgery **114**(1), 121–128 (2004).
24. U. Gehlsen, A. Oetke, M. Szaszák, N. Koop, F. Paulsen, A. Gebert, G. Huettmann, and P. Steven, "Two-photon fluorescence lifetime imaging monitors metabolic changes during wound healing of corneal epithelial cells in vitro," Graefe's Arch. Clin. Exp. Ophthalmol. **250**(9), 1293–1302 (2012).
25. Z. Mao, M. Ye, W. Hu, X. Ye, Y. Wang, H. Zhang, C. Li, and Z. Liu, "Design of a ratiometric two-photon probe for imaging of hypochlorous acid (HClO) in wounded tissues," Chem. Sci. **9**(28), 6035–6040 (2018).
26. S. C. Gnyawali, K. G. Barki, S. S. Mathew-Steiner, S. Dixith, D. Vanzant, J. Kim, J. L. Dickerson, S. Datta, H. Powell, S. Roy, V. Bergdall, and C. K. Sen, "High-resolution harmonics ultrasound imaging for non-invasive characterization of wound healing in a pre-clinical swine model," PLoS One **10**(3), e0122327 (2015).
27. S. C. Gnyawali, M. Sinha, M. S. E. Masry, B. Wulff, S. Ghatak, F. Soto-Gonzalez, T. A. Wilgus, S. Roy, and C. K. Sen, "High resolution ultrasound imaging for repeated measure of wound tissue morphometry, biomechanics and hemodynamics under fetal, adult and diabetic conditions," PLoS One **15**(11), e0241831 (2020).
28. S. Yousefi, J. J. Qin, S. Dziennis, and R. K. Wang, "Assessment of microcirculation dynamics during cutaneous wound healing phases in vivo using optical microangiography," J. Biomed. Opt **19**(7), 076015 (2014).
29. U. Baran, W. J. Choi, and R. K. Wang, "Potential use of OCT-based microangiography in clinical dermatology," Skin Res Technol **22**(2), 238–246 (2016).
30. A. J. Deegan, W. Wang, S. Men, Y. Li, S. Song, J. Xu, and R. K. Wang, "Optical coherence tomography angiography monitors human cutaneous wound healing over time," Quant. Imaging Med. Surg. **8**(2), 135–150 (2018).
31. L. V. Wang and S. Hu, "Photoacoustic tomography: in vivo imaging from organelles to organs," Science **335**(6075), 1458–1462 (2012).
32. R. Cao, J. Li, B. Ning, N. Sun, T. Wang, Z. Zuo, and S. Hu, "Functional and oxygen-metabolic photoacoustic microscopy of the awake mouse brain," NeuroImage **150**, 77–87 (2017).
33. B. Ning, R. Cao, J. Li, N. Sun, Z. Zuo, and S. Hu, "Multi-parametric photoacoustic microscopy of photothrombotic stroke in the mouse brain," in *Biomedical Optics 2016 (2016), Paper BTh3D.4* (Optical Society of America, 2016), p. BTh3D.4.
34. B. Ning, M. J. Kennedy, A. J. Dixon, N. Sun, R. Cao, B. T. Soetikno, R. Chen, Q. Zhou, K. K. Shung, J. A. Hossack, and S. Hu, "Simultaneous photoacoustic microscopy of microvascular anatomy, oxygen saturation, and blood flow," Opt. Lett. **40**(6), 910–913 (2015).
35. W. Qin, W. Qi, T. Jin, H. Guo, and L. Xi, "In vivo oral imaging with integrated portable photoacoustic microscopy and optical coherence tomography," Appl. Phys. Lett. **111**(26), 263704 (2017).
36. Z. Cheng, H. Ma, Z. Wang, and S. Yang, "In vivo volumetric monitoring of revascularization of traumatized skin using extended depth-of-field photoacoustic microscopy," Front. Optoelectron. **13**(4), 307–317 (2020).
37. S. Hu, K. Maslov, and L. V. Wang, "In vivo functional chronic imaging of a small animal model using optical-resolution photoacoustic microscopy," Med. Phys. **36**(6Part1), 2320–2323 (2009).
38. N. Sun, B. Ning, A. C. Bruce, R. Cao, S. A. Seaman, T. Wang, R. Fritsche-Danielson, L. G. Carlsson, S. M. Peirce, and S. Hu, "In vivo imaging of hemodynamic redistribution and arteriogenesis across microvascular network," Microcirculation **27**, e12598 (2020).
39. B. Ning, N. Sun, R. Cao, R. Chen, K. Kirk Shung, J. A. Hossack, J.-M. Lee, Q. Zhou, and S. Hu, "Ultrasound-aided multi-parametric photoacoustic microscopy of the mouse brain," Sci. Rep. **5**(1), 18775 (2016).
40. R. Cao, J. Li, C. Zhang, Z. Zuo, and S. Hu, "Photoacoustic microscopy of obesity-induced cerebrovascular alterations," NeuroImage **188**, 369–379 (2019).

Biomedical Optics EXPRESS

41. B. Soetikno, S. Hu, E. Gonzales, Q. Zhong, K. Maslov, J.-M. Lee, and L. V. Wang, "Vessel segmentation analysis of ischemic stroke images acquired with photoacoustic microscopy," in *Photons Plus Ultrasound: Imaging and Sensing* 2012 (SPIE, 2012), 8223, pp. 765–769.
42. J. Yao, L. Wang, J.-M. Yang, K. I. Maslov, T. T. W. Wong, L. Li, C.-H. Huang, J. Zou, and L. V. Wang, "High-speed label-free functional photoacoustic microscopy of mouse brain in action," Nat. Methods **12**(5), 407–410 (2015).
43. C. K. Sen, "Wound healing essentials: let there be oxygen," Wound Repair and Regeneration **17**(1), 1–18 (2009).
44. D. M. Castilla, Z.-J. Liu, and O. C. Velazquez, "Oxygen: implications for wound healing," Advances in Wound Care **1**(6), 225–230 (2012).
45. B. B. Mendes, M. Gómez-Florit, P. S. Babo, R. M. Domingues, R. L. Reis, and M. E. Gomes, "Blood derivatives awaken in regenerative medicine strategies to modulate wound healing," Adv. Drug Delivery Rev. **129**, 376–393 (2018).
46. R. M. Bateman, M. D. Sharpe, and C. G. Ellis, "Bench-to-bedside review: microvascular dysfunction in sepsis –hemodynamics, oxygen transport, and nitric oxide," Crit Care **7**(5), 359–373 (2003).
47. A. A. Tandara and T. A. Mustoe, "Oxygen in wound healing—more than a nutrient," World J. Surg. **28**(3), 294–300 (2004).
48. R. Ross, E. Raines, and D. Bowen-Pope, "Growth factors from platelets, monocytes, and endothelium: their role in cell proliferation," Ann. N. Y. Acad. Sci. **397**(1 Cell Prolifer), 18–24 (1982).
49. E. A. O'Toole, M. P. Marinkovich, C. L. Peavey, M. R. Amieva, H. Furthmayr, T. A. Mustoe, and D. T. Woodley, "Hypoxia increases human keratinocyte motility on connective tissue," J. Clin. Invest. **100**(11), 2881–2891 (1997).
50. R. B. Fries, W. A. Wallace, S. Roy, P. Kuppusamy, V. Bergdall, G. M. Gordillo, W. S. Melvin, and C. K. Sen, "Dermal excisional wound healing in pigs following treatment with topically applied pure oxygen," Mutation Research/Fundamental and Molecular Mechanisms of Mutagenesis **579**(1-2), 172–181 (2005).
51. H. F. Zhang, K. Maslov, G. Stoica, and L. V. Wang, "Functional photoacoustic microscopy for high-resolution and noninvasive in vivo imaging," Nat. Biotechnol. **24**(7), 848–851 (2006).
52. S. Schreml, R. m. Szeimies, L. Prantl, S. Karrer, M. Landthaler, and P. Babilas, "Oxygen in acute and chronic wound healing," British Journal of Dermatology **163**(2), 257–268 (2010).